

SHIMMER: a spatial heterodyne spectrometer for remote sensing of Earth's middle atmosphere

John M. Harlander, Fred L. Roesler, Joel G. Cardon, Christoph R. Englert, and Robert R. Conway

It is well known and demonstrated that interference spectroscopy offers capabilities to obtain passive remote optical sensing spectra of high precision and also achieves economies in size, cost, and ease of deployment compared with more conventional systems. We describe the development of a near-ultraviolet spatial heterodyne spectrometer designed for remote sensing of the global distribution of the hydroxyl radical OH in the Earth's middle atmosphere. The instrument, known as SHIMMER (Spatial Heterodyne Imager for Mesospheric Radicals), is expected to obtain its first OH measurement from space in early 2002 from the Space Shuttle. © 2002 Optical Society of America

OCIS codes: 010.1290, 120.3180, 120.6200.

1. Introduction

The instrument described in this paper draws its primary scientific motivation from the Middle Atmosphere High Resolution Spectrograph Investigation (MAHRSI), which was designed specifically to make global measurements of OH in the middle atmosphere from low Earth orbit. The importance of the hydroxyl radical OH in the photochemistry of planetary atmospheres has been recognized for more than 50 years¹; nevertheless, recent satellite observation with high-resolution ultraviolet (UV) spectroscopy has resulted in a number of unexpected results. The MAHRSI measurements provide firm evidence that the photochemistry of ozone and the odd-hydrogen HO_x family (H, OH, and HO₂) as formulated in current atmospheric models cannot consistently explain the abundance of OH throughout the middle atmosphere.^{2–4} In addition, comparisons of the MAHRSI data with direct measurements of mesospheric H₂O by the Halogen Occultation Experiment (HALOE) instrument on the Upper Atmosphere Re-

search Satellite (UARS) have revealed that the OH data also comprise a powerful measure of the distribution of mesospheric water vapor.² A layer of H₂O detected near an altitude of 65 km violates our understanding of the processes by which water is produced in and transported through the middle atmosphere. MAHRSI data also led to the discovery of a water-vapor layer near the Arctic summer mesopause, possibly related to the formation of high-altitude (82-km) polar mesospheric clouds; it has been suggested⁵ that the increasing occurrence of such clouds is a vivid indication of atmospheric change caused by human activity. However, to our knowledge, there is little quantitative knowledge of why polar mesospheric clouds form and why they vary.

In its measurement of OH, MAHRSI observed the UV solar resonant fluorescent band of OH near 308-nm wavelength with a resolving power of approximately 15,000,⁶ which was high enough to separate unambiguously the OH emission from the bright spectrally complex background formed by sunlight Rayleigh scattered by the ambient atmosphere. The MAHRSI results and the atmospheric science questions they raise clearly define the need and the requirements for a high-spectral-resolution UV instrument with high spatial resolution and high throughput. However, the weight (138 kg), size (120 cm × 85 cm × 23 cm), complexity, and responsivity of a conventional spectrograph like MAHRSI make it unsuitable for future satellite mission opportunities.

Using an innovative optical technique called spatial heterodyne spectroscopy (SHS),^{7,8} we developed

J. M. Harlander (harlander@stcloudstate.edu) is with the Department of Physics, Astronomy and Engineering Science, St. Cloud State University, St. Cloud Minnesota 56301-4498. F. L. Roesler is with the Department of Physics, University of Wisconsin-Madison, Madison, Wisconsin 53706. J. G. Cardon, C. R. Englert, and R. R. Conway are with the U.S. Naval Research Laboratory, Code 7641, Washington, D.C. 20375.

Received 9 May 2001; revised manuscript received 10 October 2001.

0003-6935/02/071343-10\$15.00/0

© 2002 Optical Society of America

an instrument called the Spatial Heterodyne Imager for Mesospheric Radicals, or SHIMMER, which appears capable of outperforming MAHRSI in a much smaller and lighter package. Extensive laboratory testing indicates that the performance of SHIMMER is near theoretical predictions. Despite its small size and great simplicity, laboratory calibrations demonstrate that the responsivity of SHIMMER [(counts/s)/(kRayleigh/nm)] is more than 10,000 times larger than MAHRSI and its spectral resolution (0.0058 nm) is 3.5 times better. Its mechanical volume and mass are approximately 17% of MAHRSI's. A proof-of-concept test flight of SHIMMER is planned from the middeck of the Space Shuttle by use of the high-quality optical window in the orbiter side hatch. Environmental tests have verified that the design is suitable for Shuttle launch environments.

In the following sections we describe the fundamental concepts, design, laboratory evaluation, history, and current status of SHIMMER.

2. Properties of Spatial Heterodyne Spectroscopy Instruments

SHS is particularly well suited to UV applications that require high resolving power and high throughput over a relatively narrow spectral band. In general, however, a spatial heterodyne spectrometer can be tuned to work in any spectral region with control over the trade-off between spectral resolution and bandwidth. SHS is similar to Fourier-transform spectroscopy (FTS), with three primary differences. First, SHS effectively heterodynes the interferogram about a selected reference wavelength, resulting in easily measurable low-spatial-frequency fringes produced by wavelengths in the passband of the instrument. Second, the spatial heterodyne spectrometer has no moving parts, even in the field-widened mode, and therefore is much smaller, lighter, and less complex mechanically than FTS instruments making similar measurements. Third, SHS uses an imaging detector to record a fringe pattern localized inside the interferometer, consequently phase errors resulting from optical defects can be easily corrected in the data reduction. Compared with more conventional grating spectrometers such as MAHRSI, SHS achieves orders of magnitude higher throughput at similar or higher spectral resolution in a much smaller package.⁸ As is the case with FTS instruments, zero, one, or two dimensions of spatial information can be obtained by appropriate choice of the optics prior to the interferometer.

A. Basic Spatial Heterodyne Spectroscopy On-Axis Analysis

The basic SHS concept is depicted in the Fig. 1, where the image of an extended scene is collimated to form a beam incident on the beam splitter. Diffraction gratings in each arm return the light to the beam splitter. Lenses L_2 and L_3 in the exit beam image the gratings onto a position-sensitive detector. The gratings are positioned so that they are the same distance from the beam splitter along the optical axis

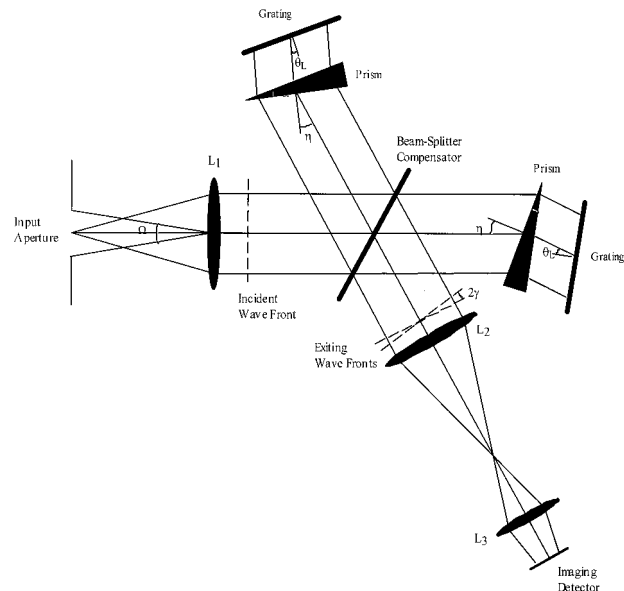


Fig. 1. Conceptual diagram of a field-widened spatial heterodyne spectrometer.

and are set at an angle θ_L such that rays of a certain wavelength incident on the gratings parallel to the optical axis retroreflect, returning parallel to the optical axis. At this wavelength, called the Littrow wavelength, the recombining wave fronts exit the interferometer completely in phase with each other combining constructively at all points across the aperture. For a wavelength slightly different from the Littrow wavelength, the diffracted beams return at a small angle to the optical axis, and the recombining wave fronts are crossed as depicted in Fig. 1. In this case the phase difference between the two wave fronts changes from a maximum at one edge, to zero in the middle, and back to maximum at the other edge, resulting in a Fizeau fringe pattern whose spatial frequency is related to the angle at which the wave fronts cross.

The off-Littrow angle γ , at which incident light parallel to the optical axis of wave number σ exits the interferometer, is given by the grating equation

$$\sigma[\sin \theta_L + \sin(\theta_L - \gamma)] = m/d, \quad (1)$$

where m is the order of diffraction, θ_L is the Littrow angle, and $1/d$ is the grating groove density. The spatial frequency of Fizeau fringes is related to the wave number of light by the equation

$$f_x = 2\sigma \sin \gamma \approx 4(\sigma - \sigma_0) \tan \theta_L, \quad (2)$$

where the approximation assumes small γ , and σ_0 is the Littrow wave number for which $\gamma = 0$. For axial rays, the intensity at the fringe localization plane for incident spectral density $B(\sigma)$ is given by

$$I(x) = \int_0^\infty B(\sigma) (1 + \cos\{2\pi[4(\sigma - \sigma_0)x \tan(\theta_L)]\}) d\sigma, \quad (3)$$

where x is measured in the dispersion plane of the gratings. Note that, except for the constant term, $I(x)$ is the Fourier transform of the input spectrum. The fringe localization plane is at the gratings, and therefore the gratings are imaged directly on the detector to produce an interferogram that is then Fourier transformed to recover the input spectrum. The maximum achievable resolving power is given by $R_0 = 4W\sigma \sin \theta_L$ where W is the width of the gratings. It can be shown that R_0 is simply equal to the total number of grating grooves imaged onto the detector.

The nonaliased passband of the spatial heterodyne spectrometer is limited by the number of samples across the interferogram. If the detector has N pixels in the dispersion plane of the gratings (the plane of Fig. 1), $N/2$ nonaliased spectral resolution elements can be measured, resulting in a passband of $N\sigma/(2R)$. To achieve this maximum bandwidth, the optics that image the gratings on the detector must adequately reproduce $N/2$ fringes at the detector.

The symmetry of the cosine interferogram in Eq. (3) results in an ambiguity between wave numbers above and below the Littrow wave number ($\sigma \pm \Delta\sigma$) as their fringe frequencies are identical. This has the effect of folding the spectrum about the Littrow wave number. This ambiguity can be handled in one of three ways: (1) The cosine symmetry can be broken by the introduction of a small tilt to one of the gratings to produce low-spatial-frequency fringes in the y dimension of the detector in addition to the wave-number-dependent fringes in the x direction illustrated in Eq. (3). With this y tilt, the resulting fringe patterns are rotated clockwise or counterclockwise depending on whether σ is above or below the Littrow wave number. A two-dimensional Fourier transform distinguishes between these fringe patterns. (2) A prefilter can be used to block light on one side of the Littrow wave number. (3) The folded spectrum can be accounted for in the spectral analysis. The prefilter solution to this problem was chosen for SHIMMER.

B. Off-Axis Analysis

When off-axis angles are included in the grating equation, it can be shown⁷ that the solid-angle field of view of the interferometer without field-widening prisms is characteristic of a conventional interferometer (Fabry-Perot or FTS) operating at the same resolving power and is given by $\Omega = 2\pi/R_0$. This limit is defined as the field of view at which, for monochromatic light, extreme rays produce one additional fringe across the detector compared with the axial rays. With the field of view limited to Ω , a monochromatic interferogram will have highest fringe contrast in the center where all fringe patterns from all angles are in phase and a slightly decreasing contrast toward the edges as the fringes become increasingly out of phase. Because of this phase difference at its edges, the envelope of the interferogram changes from a rectangular function to a rectangle multiplied by a sinc function.⁷ The resulting instrumental profile is broadened slightly and resolution is reduced

slightly as a result. A further increase in the field of view will result in reduced fringe contrast at the ends of the interferogram and an unacceptably broadened instrument function. These considerations are exactly analogous to the trade-off between field of view, fringe amplitude, contrast, and resolution in Michelson FTS.⁹

The field of view can be greatly increased through use of the field-widening prisms shown in Fig. 1. The fixed prisms serve to rotate the images of the gratings (from a geometrical optics point of view) so that they appear to be normal to the optical axis. In this configuration, the spatial-frequency dependence with an off-axis angle is minimized for monochromatic light, and fringe patterns with nearly constant contrast across the entire detector are produced even when the field of view at the gratings is increased by an order of magnitude above the non-field-widened case. Such a large field of view gives SHS an enormous throughput advantage over grating spectrometers that require a narrow slit to achieve high resolving power.

A detailed analysis of field widening shows that the field of view of the interferometer is limited by either prism spherical aberration for systems with small Littrow angles or by prism astigmatism for large Littrow angles.¹⁰ For the case of SHIMMER in which astigmatism is the limiting factor, the maximum field of view can be obtained by use of a prism at minimum deviation with angle of incidence η (see Fig. 1) given by

$$\frac{(n^2 - 1)}{n^2} \tan \eta \frac{2n^2 - \sin^2 \eta}{n^2 - \sin^2 \eta} = \tan \theta_L, \quad (4)$$

where n is the prism index of refraction. Once η is determined from Eq. (4), the prism apex angle α is given by the condition for minimum deviation through the prism:

$$n \sin\left(\frac{\alpha}{2}\right) = \sin \eta. \quad (5)$$

The field-widening prisms also introduce resolution in addition to the grating dispersion. The resulting resolving power R is given by

$$R = R_0 \left(1 - \lambda \frac{\Delta n}{\Delta \lambda} \frac{n}{n^2 - 1} \right), \quad (6)$$

where the correction to R_0 is due to dispersion by the prisms with index of refraction n at wavelength λ .

C. Spatial Imaging Considerations

Spatial heterodyne spectrometer instruments can obtain zero, one, or two dimensions of spatial information with appropriate choice of the optics prior to the interferometer. When the scene is imaged by a telescope on the input aperture, each point on the interferogram collects light from all points in the scene. In this case the interferogram represents the average spectrum over the field of view of the telescope.

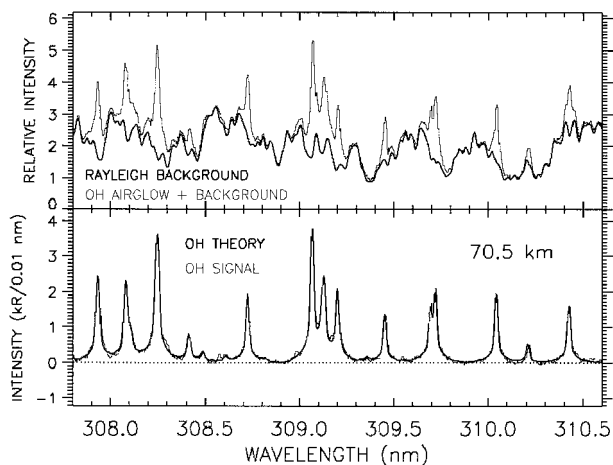


Fig. 2. MAHRSI detection of OH at 70-km tangent height.

However, when the scene is imaged on the localization plane of the fringes near the gratings, spatial as well as spectral information can be obtained. If the scene contains only one dimension of spatial information as is the case with SHIMMER (we expect the OH profiles to vary spatially only perpendicular to the Earth's limb), an interferogram for each altitude can be obtained when the detector is read out row by row. In situations in which intensity variations parallel to the limb distort the interferogram, the spatial information in this dimension can be washed out by use of an anamorphic telescope. We can obtain two-dimensional spatial information along with spectra by scanning the field of view during an observation while time tagging detected photons.^{11,12}

3. SHIMMER Instrument

A. Measurement Considerations

The SHIMMER instrument has been specifically designed to measure OH solar resonance fluorescence while viewing the limb from low Earth orbit. This measurement is a rigorous test of any hyperspectral imaging technology because retrieval of the OH radiance profile requires highly accurate knowledge of the instrument's performance. In particular, the retrieval of OH spectra from limb observations entails identification and removal of the bright and spectrally complex ozone-attenuated Rayleigh-scattered solar background. This is accomplished when we perform a nonlinear least-squares curve-fitting procedure that relies on high-spectral-resolution measurements to properly identify and separate the spectral components of the limb observations. Direct measurements of the Moon with a diffuser are used to determine the solar background spectral shape measured by SHIMMER independent of terrestrial OH emission.

The problem is illustrated in Fig. 2, where the top panel shows a MAHRSI-measured OH emission spectrum at 70-km tangent height and the underlying Rayleigh-scattered solar spectrum. This is the tangent altitude for which OH is most prominent against

the Rayleigh-scattered solar background. The lower panel shows the OH signal extracted when the Rayleigh background is subtracted from the raw spectrum. Because, in effect, the curve-fitting algorithm subtracts one large number from another at every wavelength, leaving the residual OH spectrum, any uncharacterized and uncorrected instrumental contributions to the spectral shape will result in large errors in the retrieved OH intensity, particularly for observations of lower tangent heights. The error in the fit of the background shape is greatly reduced when we utilize the full bandwidth of the spectral region of the OH fluorescence. It is the combination of high spectral resolution and extended bandwidth that is essential to the accurate identification of the background spectrum contribution. Furthermore, as the altitude intensity profiles are inverted to yield OH concentration profiles, the intensity errors propagate through the inversion to produce even larger concentration uncertainties. For example, large retrieval and inversion errors will be generated if knowledge of the instrument function and its variation with wavelength or position in the observed scene is incomplete or inaccurate, if the spectral responsivity of the instrument is not well characterized, or if off-axis or internally scattered light is not controlled adequately. The design specifications for the SHIMMER instrument are summarized in Table 1. The spectral resolution, passband, field of view, and responsivity requirements of SHIMMER were determined by the previous successful OH measurements by the MAHRSI instrument.

The optical layout is shown schematically in Fig. 3. The 500-mm focal-length refractive telescope focuses the sky on the gratings. The telescope objective diameter limits the range of angles incident on the gratings while also imaging the scene at infinity on the grating localization plane. This property will be used in SHIMMER to image altitude along the columns of the CCD while producing one-dimensional interferograms along the rows while limb viewing from space. Telescope aberrations limit the altitude resolution on the limb to 0.87 km. In practice, however, rows will be coadded on the chip to give a 2.2-km (4.3-arc min) altitude resolution.

Out-of-band rejection is achieved by a 6.6-cm-diameter interference filter between the telescope and the interferometer and narrow-band multilayer dielectric coatings on the three fold mirrors in the system. All transmitting elements have been anti-reflection coated for 308 nm. The interference filter has a 2.3-nm FWHM passband centered at 308.9 nm. Because the interferometer in this design cannot distinguish between wavelengths at $+\Delta\lambda$ and $-\Delta\lambda$ about the Littrow wavelength, the violet edge of the filter passband is positioned near the Littrow wavelength (307.0 nm) so that shorter wavelengths are blocked. The interferometer uses an antireflection-coated, nonpolarizing hexagonal beam splitter, a pair of 13.02° apex angle field-widening prisms, and a pair of 1200 lines/mm, 75% efficiency gratings. For fused-silica prisms, 1200-line/mm gratings, and a design

Table 1. SHIMMER Design Specifications

Aspect	Attribute	Design
System	Interference filter	2.3-nm FWHM centered at 308.9 nm
		307.0–310.5-nm full width
	Entrance optics	500-mm focal-length telescope
	Exit optics	7-element relay system
	Detector	1034 × 1024 24 μm × 24 μm CCD
	Gratings	
	Clear aperture	20 mm × 20 mm
	Groove density	1200 lines/mm
	Littrow angle	10.7°
	Littrow wavelength	307.0 nm
	Field-widening prisms	
	Clear aperture	22 mm × 22 mm
	Wedge angle	13.02°
	Incident angle	8.73°
	Exit angle	10.7°
	Beam splitter	
	Clear aperture	28 mm × 28 mm
	Field of view	
	At gratings	10°
	On sky	2.3 × 2.3°
Performance	Resolving power	53,500
	Spectral resolution	0.0058 nm
	Nonaliased spectral range	2.95 nm
	Achieved spectral range	Filter limited
	Sky imaging	1.7 arc min
Resources	Mass	22 kg
	Volume	47 cm × 36 cm × 24 cm
	Power	27 W
	CCD readout	72 bytes/8 s
	Image rate	375 images/orbit
	Data rate	27 Mbytes/orbit

wavelength of 308.5 nm, the Littrow angle of the grating and the optimal angle of refraction of the optical axis leaving the prism are nearly equal [see Eqs. (1)–(3) in Section 2.A]; hence the back face of the prisms and the gratings are nearly parallel. For ease of alignment the back prism face and the grating face were made parallel for SHIMMER (see Table 1). A doublet field lens and a multielement relay lens focus the plane of the gratings, which is the fringe localization plane, on the CCD. The theoretical modulation transfer function (MTF) of the SHIMMER imaging lenses is shown in Fig. 4.

The camera used in SHIMMER utilizes a thinned backilluminated UV antireflection-coated CCD manufactured by Scientific Imaging Technologies Inc. with approximately 58% quantum efficiency at 308 nm. The CCD format is 1024 × 1024 with 24 μm × 24 μm pixels. The camera also includes a shutter mechanism, thermoelectric coolers, cooling fins, and fans to convectively dispel heat into the cabin air.

The mechanical design for SHIMMER was driven by five requirements: (1) locate and support to in-

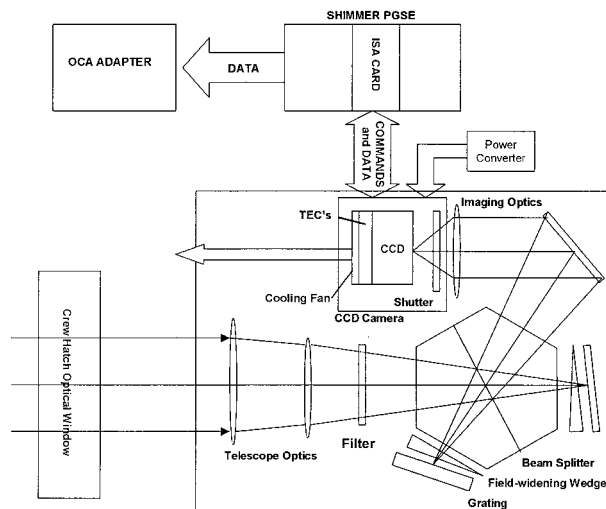


Fig. 3. SHIMMER block diagram and optical layout. OCA, orbiter communication adapter; ISA, industry-standard architecture-bus computer; PGSE, payload and general support electronics; TEC, thermoelectric cooler.

terferometric precision the optical elements of the interferometer in a manner suitable for Space Shuttle launch and landing loads; (2) locate and fasten the optical components shown in Fig. 3 to ensure accurate alignment; (3) constrain the mechanical envelope of the instrument to the interior dimensions of the Space Shuttle middeck lockers; (4) provide a simple, robust mating assembly to locate and fasten the instrument to the Space Shuttle crew hatch; and (5) meet all manned-flight program safety requirements.

The interferometric elements, i.e., the beam splitter, prisms, and gratings, are mounted in a VascoMax steel structure shown in Fig. 5 and labeled interferometer in Fig. 6. The beam splitter is positioned below the triangular cap visible at the top, and the input and output windows are on the backside. The

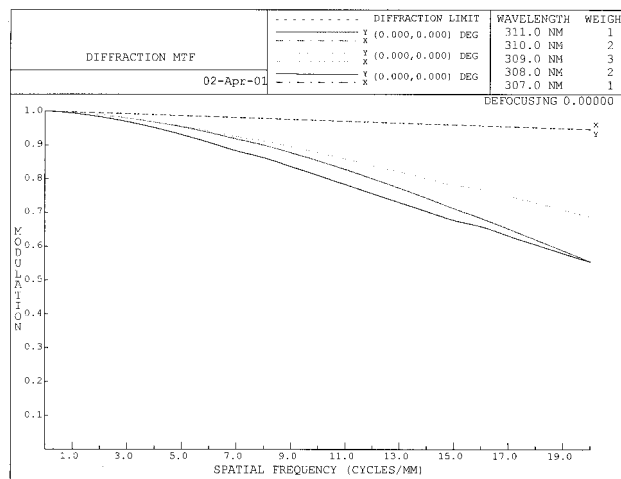


Fig. 4. Theoretical exit optics MTF. The three solid curves are for on-axis, 70% field and full field points on the gratings. The dashed curve shows the diffraction-limited MTF. The pixels on the CCD limit the maximum frequency to 21 cycles/mm.

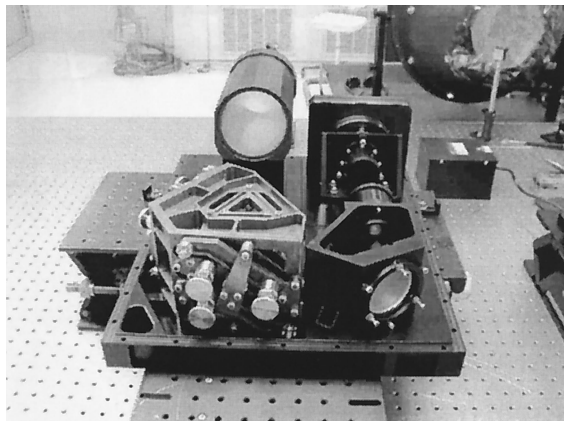


Fig. 5. SHIMMER components on the flight baseplate in the laboratory.

design allows precise and stable positioning of the prisms and gratings relative to the beam splitter. The prism holders are attached to the grating holders, and a spring-loaded turret assembly holds the grating holders tightly to a three-point kinematic mount integral to the cell structure. An interior chamber encloses the CCD camera and is walled off by light-tight bulkheads and baffle tubes. Both air-flow apertures open into this isolated space. Each aperture is covered by a 50- μm mesh screen. The entrance aperture is protected by a transparent Lexan cover that will be removed on orbit by the flight crew. The cover plate of the housing unit also provides attach points for lifting the handles.

B. Operational Considerations

As described above, SHIMMER was designed to conduct a spaceflight proof test of the application of the SHS technique to remote sensing of the middle atmosphere. The test will be to observe the vertical profile of OH solar resonance fluorescence when the Earth's Sun-illuminated horizon is imaged through the UV-transmitting optical window in the Space Shuttle orbiter crew hatch. Tests on three Shuttle windows have shown that the panes are not flat

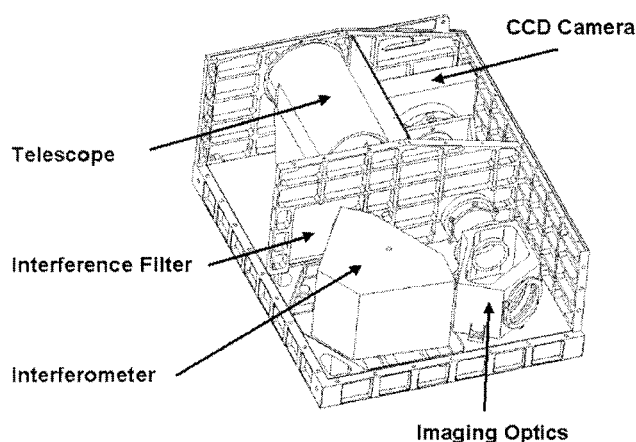


Fig. 6. SHIMMER component layout.

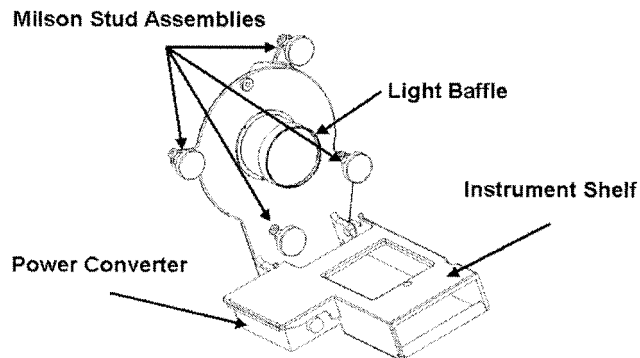


Fig. 7. SHIMMER bracket assembly.

enough to cause additional interference effects in SHIMMER interferograms. The instrument is attached to the orbiter crew hatch with a bracket assembly that utilizes a circle of threaded studs located around the optical window. As shown in Fig. 7, the bracket includes a hinged channel that supports the instrument and a power converter module. The assembly is hinged to permit folded stowage in a mid-deck locker.

The crew will maneuver the orbiter to an attitude that will place the SHIMMER line-of-sight tangent to the limb at a nominal altitude of 65 km while placing the window out of the Sun's direct illumination. The projected 2.3 deg instrument field of view will then have an upper boundary at 100-km altitude and a lower boundary at 30-km altitude. At a wavelength of 308 nm, the vertical radiance profile of Rayleigh-scattered sunlight has a well-defined maximum at approximately 41-km altitude. The flight crew will confirm the pointing of the instrument by observing the placement of this radiance peak in the field of view displayed on a laptop computer. The crew then will initiate several sequences of nominal (1.2-s) exposures. The data will be downlinked in near real time to an operations control center at Johnson Space Center where the SHIMMER science team will analyze the data and provide feedback to the crew. After the flight, the data will be analyzed to produce OH number density profiles by use of algorithms validated in the laboratory and on MAHRSI data.

4. Instrument Characterization in the Laboratory

An extensive series of laboratory tests have verified that SHIMMER has met design expectations. The most basic test is to observe the interferogram produced by a monochromatic source within the instrument's spectral filter passband ($\%T > 35\%$ from 307.8 to 309.6 nm). A Zn pen-ray lamp with a single bright emission at 307.6 nm was used for optimization and testing. The spectral width of the emission is not resolved by the interferometer. The fringe pattern recorded by SHIMMER with the Zn pen-ray source is shown in Fig. 8. Note that all spectral information is in the horizontal dimension, and the vertical dimension is exclusively an image of the vertical intensity distribution of the source. When ap-

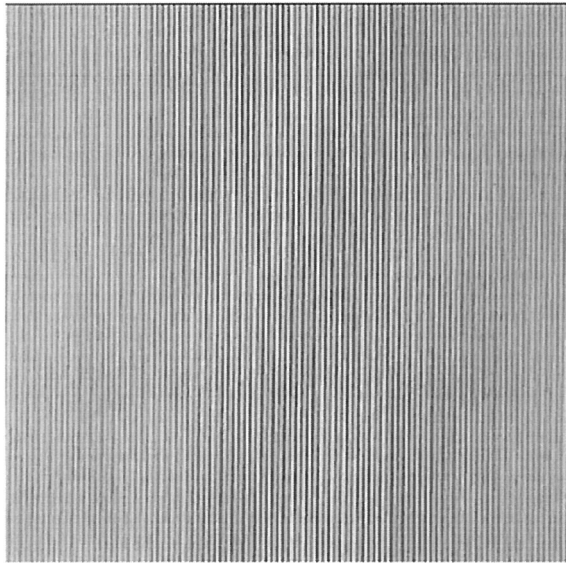


Fig. 8. Interferogram recorded in the laboratory.

plied to the OH limb-viewing problem, the vertical dimension will be aligned perpendicular to the limb so that each row of the CCD will record the spectrum observed at distinct viewing angles corresponding to distinct tangent heights.

As discussed in Section 2.A, grating figure errors and interferometer refractive-index inhomogeneities distort the Fizeau fringe pattern recorded at the CCD, but with the high-quality optics of SHIMMER, these distortions are negligible. The interferogram was corrected for dark field and nonuniformity, then Fourier transformed to produce the spectrum shown in Fig. 9. Because the Zn line at 307.6 nm is unresolved by the instrument, this spectrum represents the achieved instrument function.

The passband of the instrument is determined by the spectral filter, the spectral resolution, the number of pixels sampling the interferogram, and the image quality at the CCD. In these tests, we focused the

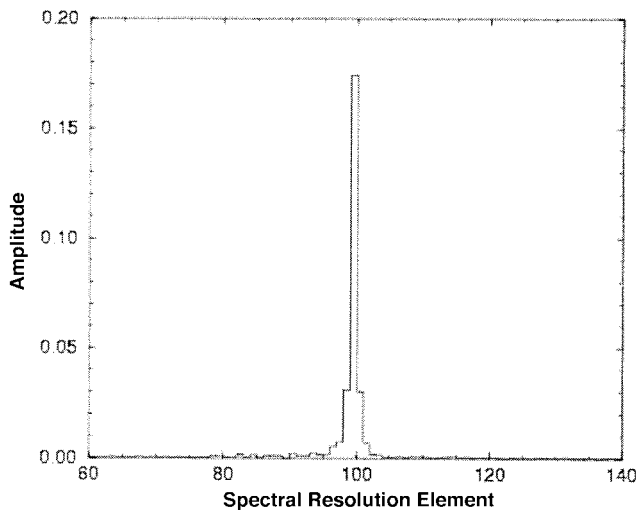


Fig. 9. Measured Zn emission feature at 307.6 nm.

image of the gratings onto 1024 pixels, so the number of spectral elements available without aliasing is 512. Assuming perfect imaging, the maximum passband should be 512 times the spectral resolution (0.0058 nm as verified by means of OH emission as described below), or approximately 3.0 nm.

Tests with a polychromatic source were conducted with a microwave-excited OH lamp. These tests verified that the spectral resolution, bandwidth, and field of view all meet design specifications. With the gratings adjusted for a Littrow wavelength of 306.42 nm, the OH spectrum shown in the first panel of Fig. 10 was recorded. We generated the spectrum in the second panel using OH g factors assuming a solar source and a rotational temperature of 2000 K. Figure 10 shows that the two features at 307.526 and 308.607 nm are recorded in spectral resolution elements 213 and 395. This coupled with the one-pixel-wide line shape in the Zn spectrum in Fig. 9 verify a spectral resolution of 0.0059 nm, or a resolving power of 53,500 as designed. The second panel shows the OH spectrum and filter transmission folded about the Littrow wavelength of 306.42 nm. As mentioned above, the interferometer cannot distinguish between wavelengths at $+\Delta\lambda$ and $-\Delta\lambda$ about the Littrow wavelength, but, because the short-wavelength edge of the filter passband is near the Littrow wavelength, the wavelengths to the violet of Littrow are blocked.

We measured the average spectral responsivity of the instrument using a calibrated Labsphere Inc. integrating sphere with an 8-in.- (20-cm-) diameter aperture, internal Spectralon diffuse reflecting tiles, and multiple halogen lamp sources. The absolute spectral radiance of the sphere was measured at the NASA Goddard Space Flight Center Laboratory for Atmospheres in collaboration with the Shuttle Solar Backscatter Ultraviolet experiment team.^{13,14} The SHIMMER field-of-view footprint is within the sphere's aperture. The total signal at the CCD (digital number, DN) is related to the total inband photon flux at the SHIMMER input aperture by

$$S(\text{DN}) = \phi(\text{phot/s})\tau_{\text{int}}(\text{s})\bar{T}_{\text{filt}}\bar{T}_{\text{opt}}QE_{\text{CCD}}(e^-/\text{phot}) \times G(\text{DN}/e^-), \quad (7)$$

where τ_{int} is the exposure time, \bar{T}_{filt} and \bar{T}_{opt} are the average spectral filter and optical element transmission over the passband of the instrument, and QE_{CCD} and G are the quantum efficiency and gain of the CCD. The total inband photon flux ϕ is related to the spectral radiance of the integrating sphere L_λ [in kiloRayleighs (kR) per nanometer] by

$$\phi(\text{phot/s}) = L_\lambda (\text{kR/nm}) \frac{10^9}{4\pi} \Delta\lambda(\text{nm}) A(\text{cm}^2) \Omega(\text{sr}), \quad (8)$$

where $\Delta\lambda$ is the bandwidth, A is the input aperture area, and Ω is the field of view. The measured responsivity of SHIMMER is $R = 4.34 \times 10^4 \text{ DN s}^{-1} \text{ kR}^{-1}$, the derived optical transmission is $\bar{T}_{\text{opt}} = 0.18$,

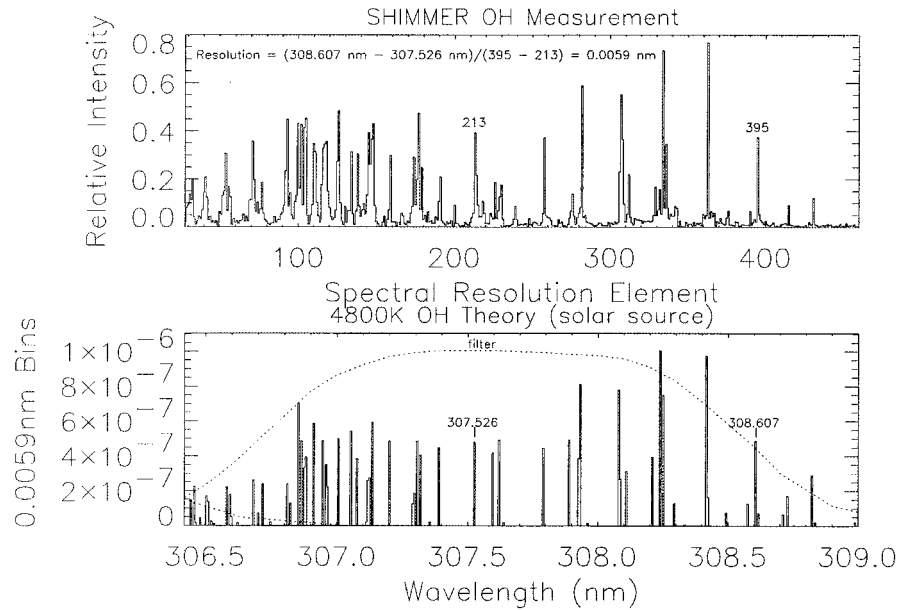


Fig. 10. OH spectrum measured in the laboratory compared with the theoretical OH spectrum.

and the calculated throughput is $\bar{T}_{\text{opt}}\bar{T}_{\text{filt}}A\Omega = 4.5 \times 10^{-3}$, all meeting instrument design goals.

5. SHIMMER Earth Limb Measurement Simulation

Model interferograms were generated to predict the performance of the instrument while viewing the limb from space. High-resolution OH g factors, solar spectrum, and spectral filter contributions are combined to produce an effective incident spectrum. The CCD rows representing a 1.2-s integration were binned into 32 row slices to increase the signal-to-noise ratio, with the OH and solar contributions appropriately weighted based on MAHRSI measurements of OH and Rayleigh-scattered background intensity collected during the STS-85 Shuttle mission. Assuming a unit power image of the gratings at the CCD, the DN's per pixel per slice [DN(pixel/slice)] that are due to altitude-dependent spectral radiances L_{OH} and L_{sun} (kR) are calculated with the equation,

$$S_{\text{CCD}}(i, j) = \int_{y(j)}^{y(j+1)} \int_{x(i)}^{x(i+1)} \int_0^\infty L_{\text{OH}}(\sigma, y) R(\sigma) \times (1 + \cos\{2\pi[4(\sigma - \sigma_0)x \tan \theta]\}) d\sigma dx dy + \int_{y(j)}^{y(j+1)} \int_{x(i)}^{x(i+1)} \int_0^\infty L_{\text{sun}}(\sigma, y) R(\sigma) \times (1 + \cos\{2\pi[4(\sigma - \sigma_0)x \tan \theta]\}) d\sigma dx dy \quad \text{DN(pixel/slice),} \quad (9)$$

where i is the CCD pixel number along rows; j is the slice number corresponding to one of 32 tangent height altitudes in the range 30–94 km; $x(i)$ and $y(j)$ are the location on the grating imaged onto the corner of the CCD region (i, j) ; and the responsivity $R(\sigma)$ that incorporates entrance aperture size, pixel field of view, optical transmission, CCD quantum efficiency,

integration time, and analog-to-digital converter gain converts radiance at the limb (kR) to signal readout from the CCD camera [DN(pixel/slice)]. Figure 11 shows the interferogram produced by anticipated OH emissions and Rayleigh-scattered sunlight. The emissions from lower altitudes, approximately a factor of 40 brighter than those from higher altitudes, are imaged at the bottom of the CCD. The line at zero optical path difference, at which the frequency components that are due to all wavelengths and incidence angles are in phase, is evident in the central column. The upper panel shows the signal (solid curves) and noise (dashed curves) components present in the interferogram at the CCD that are due to atmospheric emissions and instrumental effects. All the curves shown in the upper panel are in units of DN(pixel/slice). These curves indicate the relative contribution to the interferogram as a function of altitude for each of the signal and noise sources. Note that the total signal and noise are dominated by Rayleigh-scattered background at all altitudes. Note also that instrumental noise contributions are only significant above approximately 85 km and that the total noise becomes comparable to or dominates the OH signal only above 85 km and below 40 km.

We made estimates of the signal-to-noise ratio at each altitude by retrieving OH intensity as a function of altitude from the interferogram in the same way as will be done during the mission. In this procedure we subtract the dark-field, flat-field calibration to radiance units; Fourier transform, phase correct and perform a nonlinear curve fitting to remove the Rayleigh-scattered background; and integrate over the OH features. The bottom panel shows the retrieved OH spectral features (horizontal) as a function of altitude (vertical). The retrieved radiance as a function of altitude (shown in Fig. 12) is the same as the radiance profile input to the instrument model in

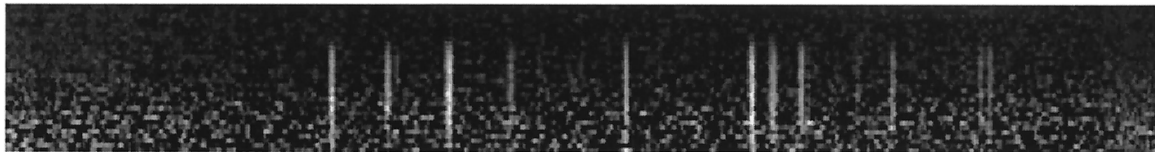
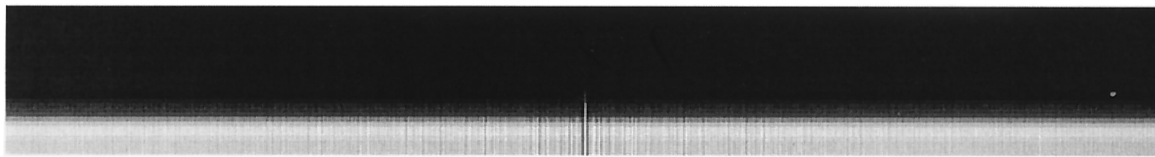
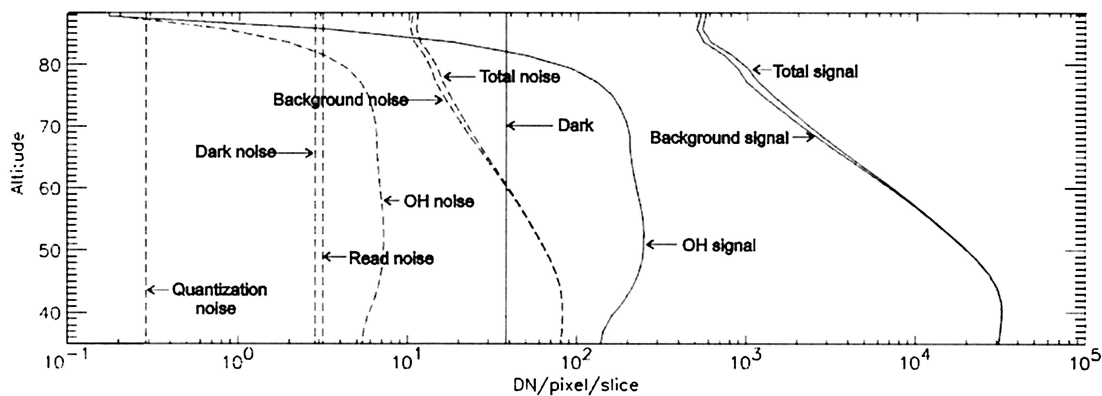


Fig. 11. (upper panel) Modeled signal and noise contributions, (middle panel) 1024×32 pixel interferogram, and (lower panel) 512×32 spectral resolution element retrieved OH.

the first place, as it should be. The estimated precision of the measurement as a function of altitude (shown in Fig. 13) is determined not only by the signal-to-noise ratio in the interferogram, but also by the bandwidth and spectral shape of the incident spectrum.

6. Future Developments

We are currently pursuing further miniaturization of an OH spatial heterodyne spectrometer with the sup-

port of NASA's Planetary Instrument Definition and Development Program. Further reduction in instrument size and weight will be achieved when the interferometer components are optically contacted to form a monolithic interferometer. This technique makes the complex VascoMax structure, which is used in SHIMMER to hold the optical components in precise proximity, obsolete. Furthermore, the alignment of a monolithic interferometer is virtually impervious to vibrations, resulting in a major risk

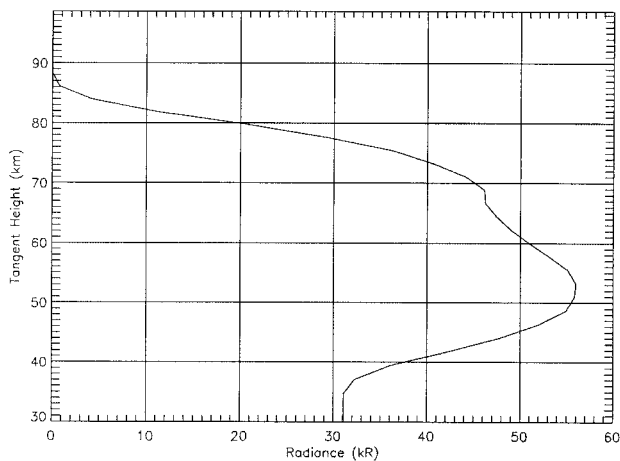


Fig. 12. Modeled OH altitude intensity profile.

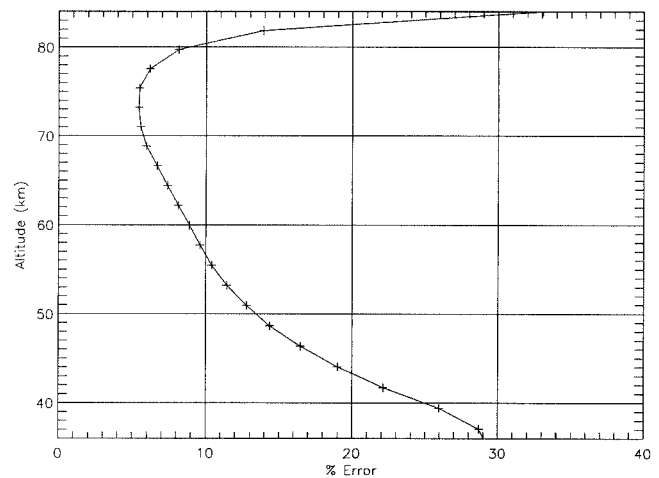


Fig. 13. Estimated OH radiance measurement precision.

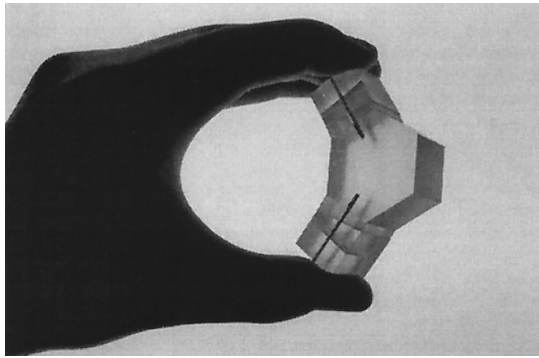


Fig. 14. Full-scale model of a miniature monolithic version of SHIMMER.

reduction for spaceflight applications. Figure 14 shows a photograph of the monolithic instrument presently under construction. It will have 200 times the throughput of MAHRSI and a spectral resolution of 0.012 nm. We plan to report on the performance of the monolithic instrument in the near future.

The latest achievements in SHS and the ongoing research confirm that this technique is remarkably well suited for the investigation of planetary atmospheres from space. For example, longstanding issues such as the polar mesospheric cloud phenomenon on Earth or the detailed understanding of the photochemistry in the Martian atmosphere can be addressed with global [OH], [NO], and temperatures provided by high-spectral-resolution UV limb spectra acquired from an orbiting platform.

The authors acknowledge Mike Stevens and Charles Brown at the U.S. Naval Research Laboratory (NRL) and also Lee Potratz at the University of Wisconsin-Madison for his assistance in the fabrication of SHIMMER. This research is supported by grants ATM-9612228 from the National Science Foundation, the Planetary Instruments Definition and Development Program of NASA's Office of Space Science, and the U.S. Air Force Space Test Program. Part of this research was performed while C. Englert held a National Research Council and NRL Research Associateship.

References

1. D. R. Bates and M. Nicolet, "The photochemistry of atmospheric water vapor," *J. Geophys. Res.* **55**, 301–327 (1950).
2. M. E. Summers, R. R. Conway, D. E. Siskind, D. Offermann, P. Preusse, and J. M. Russel, "Implications of satellite OH observations for middle atmospheric H₂O and ozone," *Science* **277**, 1967–1970 (1997).
3. R. R. Conway, M. E. Summers, M. H. Stevens, J. G. Cardon, P. Preusse, and D. Offermann, "Satellite observations of upper stratospheric and mesospheric OH: the HO_x dilemma," *Geophys. Res. Lett.* **17**, 2613–2626 (2000).
4. M. E. Summers and R. R. Conway, "Insights into middle atmospheric hydrogen chemistry from analysis of MAHRSI OH observations," *Geophys. Monogr. Am. Geophys. Union* **123**, 117–130 (2000).
5. G. E. Thomas, "Mesospheric clouds and the physics of the mesopause region," *Rev. Geophys.* **29**, 553–575 (1991).
6. R. R. Conway, M. H. Stevens, C. M. Brown, J. G. Cardon, S. E. Zasadil, and G. H. Mount, "The Middle Atmosphere High Resolution Spectrograph Investigations," *J. Geophys. Res.* **104**, 16327–16348 (1999).
7. J. Harlander, "Spatial heterodyne spectroscopy: interferometric performance at any wavelength without scanning," Ph.D. dissertation (University of Wisconsin-Madison, Madison, Wis., 1991).
8. J. Harlander, R. J. Reynolds, and F. L. Roesler, "Spatial heterodyne spectroscopy for the exploration of diffuse interstellar emission lines at far ultraviolet wavelengths," *Astrophys. J.* **396**, 730–740 (1992).
9. J. W. Brault, "Fourier transform spectroscopy," in *High Resolution in Astronomy: Fifteenth Advanced Course of the Swiss Society of Astronomy and Astrophysics*, A. Benz, M. Huber, and M. Mayor, eds. (Geneva Observatory, Sauverny, Switzerland, 1985), pp. 1–61.
10. J. M. Harlander and F. L. Roesler are preparing a manuscript to be called "Spatial heterodyne spectroscopy."
11. J. M. Harlander, H. T. Tran, F. L. Roesler, K. P. Jaehnig, S. M. Seo, W. T. Sanders, and R. J. Reynolds, "Field-widened spatial heterodyne spectroscopy: correcting for optical defects and new vacuum ultraviolet performance tests," in *EUV, X-Ray and Gamma-Ray Instrumentation of Astronomy V*, O. H. Siegmund and J. V. Vallergera, eds., *Proc. SPIE* **2280**, 310–319 (1994).
12. B. W. Smith and J. M. Harlander, "Imaging spatial heterodyne spectroscopy: theory and practice," in *Infrared Technology and Applications XXV*, B. F. Andresen and M. S. Scholl, eds., *Proc. SPIE* **3698**, 925–931 (1999).
13. E. Hilsenrath, D. E. Williams, R. T. Caffrey, R. P. Cebula, and S. J. Hynes, "Calibration and radiometric stability of the Shuttle Solar Backscatter Ultraviolet (SSBUV) experiment," *Metrologia* **30**(4), 243–248 (1993).
14. S. Janz, E. Hilsenrath, J. Butler, D. F. Heath, and R. P. Cebula, "Uncertainties in radiance calibrations of backscatter ultraviolet (BUV) instruments," *Metrologia* **32**(6), 637–641 (1996).